THE JOURNAL OF PHYSICAL CHEMISTRY C
A JOURNAL OF THE AMERICAN CHEMICAL SOCIETY

pubs.acs.org/JPCC
Article

Strain Effects on the Adsorption of Water on Cerium Dioxide Surfaces and Nanoparticles: A Modeling Outlook

Sidra Munir,* Khoa Minh Ta, Thomas Smith, Lisa J. Gillie, David J. Cooke, Stephen C. Parker, and Marco Molinari*

Cite This: J. Phys. Chem. C 2024, 128, 18451−18464
Read Online

ABSTRACT: Nanocrystalline ceria exhibits significant redox activity and oxygen storage capacity. Any factor affecting its morphology can tune such activities. Strain is a promising method for controlling particle morphology, whether as core@shell structures, supported nanoparticles, or nanograins in nanocrystalline ceria. A key challenge is to define routes of controlling strain to enhance the expression of more active morphologies and to maintain their shape during the lifespan of the particle. Here, we demonstrate a computational route to gain insights into the strain effects on particle morphology. We use density functional theory to predict surface composition and particle morphology of strained ceria surfaces, as a function of environmental conditions of temperature and partial pressure of water. We find that adsorbed molecular water is not sufficient to shift stability and as such under all compressive and tensile strains studied, the most stable particle is of octahedral shape, similarly to the unstrained case. When dissociative water is involved at the surfaces of the particle, then the most stable particle morphology changes under high water coverage and tensile strain to cuboidal or truncated cuboidal shapes. This shift in shape is due to strain effects that affect the strength of water adsorption.

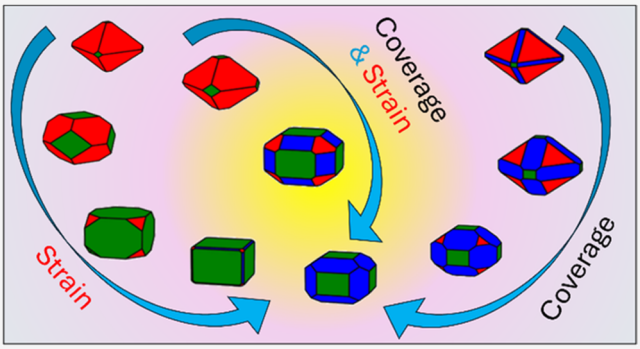

INTRODUCTION

Cerium dioxide (CeO_2) is catalytically active and has a high ionic conductivity, which makes it an ideal and effective material in catalysis and energy applications. As a catalyst, CeO_2 has found applications in reforming, three-way catalysts, and oxidation of volatile organic compounds, while as a solid electrolyte, it has found applications in solid oxide fuel cells.[1,2] Biomedical applications are the latest development and show the flexibility of CeO_2, as it displays enzyme mimetic activities such as superoxide dismutase and catalase.[3,4]

CeO_2 is an oxygen buffer (i.e., generation of oxygen vacancies) with redox activity (i.e., Ce^{3+}/Ce^{4+}). Any factor that can tweak such equilibria has the potential to inherently change the materials properties. Strain is an efficient method to attain remarkable performance in nanomaterials.[5] In particular, lattice strain is an effective method for increasing oxygen storage capacity in ultrathin $CeO_{2-\delta}$, ionic conductivity in $Gd_{0.1}Ce_{0.9}O_{2-\delta}/Er_2O_3$[6] and 8YSZ/$CeO_2$[7] films, and in La/Gd/Yb substituted CeO_2,[8] electronic transport in Pt/$BaTiO_3$/CeO_2 films,[9] enhancing catalytic properties of PdCu/CeO_2[10] and CeO_2/Mn_3O_4[11] nanocrystals, and nanozymatic activity of ultrathin CeO_2 antioxidants.[12]

Lattice strain is inevitable in supported films and in core@shell structures. It occurs at an interface due to the lattice mismatch of two different materials (heterogeneous interface), or of two surfaces of the same material (homogeneous interface). Coherent interfaces form when strain can be accommodated, and the two materials remain single crystals. There is however a critical point beyond which lattice strain is released via the formation of lattice defects, defect clustering, dislocations and interfaces or grain boundaries, forming incoherent interfaces.[13]

Most of the information on strained CeO_2 is related to supported films as they are synthesized with greater experimental control. However, contrasting findings do not provide an unambiguous relationship between lattice strain and a material's properties, hindering the design of effective strained catalysts.

In single-crystalline strained nanofilms of ∼3 nm thickness, CeO_2(100)/STO(001) (2.1% strain) and CeO_2(100)/YSZ-(001) (−5.6% strain), both tensile and compressive biaxial strain induce a tetragonal distortion, with a 4-fold increase in the concentration of Ce^{3+} following a decrease in the energy of

Received: June 23, 2024
Revised: October 7, 2024
Accepted: October 8, 2024
Published: October 17, 2024

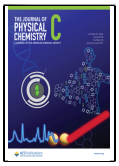

https://doi.org/10.1021/acs.jpcc.4c04172
J. Phys. Chem. C 2024, 128, 18451−18464

formation of oxygen vacancies (Vo).[14] Although compressive strain does not favor clustering of Vo in CeO_2(111)/Pt(111) (−1.3% strain),[15] self-assembly of Vo is seen in CeO_2/Rh(111) films (−1.5% strain) under reducing atmospheres, most likely from the strain-induced reduction in the formation energy of Vo.[16]

Density functional theory (DFT) calculations involving strained CeO_2 are mainly focused on the formation of Vo. Compressive strain destabilizes and tensile strain stabilizes Vo formation,[17] as the latter can easily accommodate Vo.[18] The electronic density of states show that compressive/tensile strain results in an upshift/downshift of the Ce 4f-band, which underlies the destabilization/stabilization of Vo formation.[19] Tensile strain induces a narrowing of the band gap of both bulk CeO_2[20] and the {111} stoichiometric surface,[21] while in the latter, compressive strain has the opposite effect. The narrowing of the band gap is also seen in reduced unstrained CeO_2 bulk due to the formation of Ce^{3+} and Vo, which induce lattice expansion.[22]

Compressive strain increases the water splitting reaction (WSR) activity of CeO_2 as well as reducing the free energy of formation of surface hydroxyl groups.[23] Indeed, oxygen vacancies and hydroxyl groups are stabilized by tensile strain but destabilized by compressive strain. Again, this is due to a downshift of the Ce 4f orbital energy under tensile strain, which can accommodate the larger size of Ce^{3+} ions compared to Ce^{4+} ions.[23] Tensile strain increases the reactivity of the CeO_2(111) surface, by either lowering the diffusion barrier of oxygen vacancies or increasing the reactivity toward water splitting.[24]

To map the stability of CeO_2 surfaces under varying strains, we present an extensive modeling study on the interaction of water on CeO_2 surface. We couple this with a thermodynamic strategy by generating phase diagrams to evaluate the strained structures under different temperature and pressures. This provides insights into strain effects in ultrathin nanoparticles (NPs), NPs supported on thin films, and core@shell structures, which will advance the design of more efficient strained nanocatalysts and nanozyme.

METHODOLOGY

Density functional theory (DFT) spin polarized calculations were carried out using the Vienna *Ab initio* Simulation Package (VASP).[25] The calculations used a plane wave basis set with a cutoff energy of 500 eV, and the core−valence interaction represented using the projector augmented wave (PAW) approach.[26] The frozen core is [He] for O and [Xe] for Ce. The exchange−correlation functional was the GGA Perdew−Burke−Ernzerhof for solids (PBEsol),[27] with the inclusion of the Hubbard correction parameter using the Dudarev methodology.[28] A U = 5 eV was selected to aid localization of the 4f electrons as in previous studies.[26,29−34]

Bulk CeO_2. Bulk CeO_2 was minimized with electronic and ionic criteria of 10^{-6} eV per atom and 10^{-2} eV Å^{-1}. K-point sampling of the Brillouin zone uses the Γ-centered 5 × 5 × 5 k-mesh. The 4 unit (CeO_2) minimized bulk cell gave a lattice constant of 5.497 Å, which is a known overestimation of the experimental value of 5.411 Å.[31]

CeO_2 Surfaces. The {100}, {111}, and {110} surfaces were generated using the METADISE code[35] from the minimized bulk CeO_2. The slab method was used so that the top and bottom of the configurations are identical. A vacuum gap of 15 Å was introduced perpendicular to the surface plane, which minimizes interactions between unit cells. The {100} and {111} slabs with ($\sqrt{2} \times \sqrt{2}$) and the {110} slab with ($2 \times \sqrt{2}$) expansions of the primitive surface unit cell were investigated. The {100} and {110} surfaces were 7 layers (28 CeO_2 units) and the {111} was 5 layers (20 CeO_2 units). The dipole moment of the {100} surface is removed by transferring half of the oxygen from the top to the bottom of the slab resulting in a zero net dipole moment. The Brillouin zone was sampled using a Monkhorst−Pack Γ-centered 2 × 2 × 1 k-point grid with the third vector perpendicular to the surface plane. The criteria for electronic and ionic convergence were 10^{-6} eV per atom and 10^{-2} eV Å^{-1}. When all attempts to stabilize specific configurations failed, they were run with lower electronic and ionic criteria of 10^{-4} eV per atom and 10^{-1} eV Å^{-1}, respectively. These include: {100}S-2$5H_2O$-M (4 to 5%), {110}S-2$5H_2O$-M (4 to 5%), {111}S-2$5H_2O$-M (4 to 5%), {100}S-5$0H_2O$-D(−4 to −5%), {100}S-5$0H_2O$-M (1.5 to 5%), {100}S-7$5H_2O$-M (−5 to 5%), {100}S-10$0H_2O$-M (0.5 to 5%), {111}S-5$0H_2O$-M (2.5 to 5%), {111}S-7$5H_2O$-D (−3 to −5%), {111}S-7$5H_2O$-M (3 to 5%). Note that generally they are at very high or low strain, apart from {100}S-7$5H_2O$-M and {100}S-10$0H_2O$-M, where we noted that this was the only way to stabilize the molecular form of all water molecules adsorbed at the same time at the top and bottom of the slab.

Molecule. The isolated H_2O molecule was minimized using the Γ point in a cubic cell of 1000 Å^3. Criteria for convergence were the same as for the surfaces.

Water Adsorption on CeO_2. Water was adsorbed dissociatively as hydroxyl groups and associatively as molecular H_2O. There is no change in magnetization of Ce atoms in the slab upon adsorption of dissociative water. The water molecule was symmetrically adsorbed on both the top and bottom surfaces of the slab. Different water coverages were investigated (25, 50, 75%) up to the monolayer (100%) adsorption, which corresponds to one water molecule per surface CeO_2 unit. There are a number of ways that water can be placed on the surface, but we have limited ours to structures that maximize the coordination between the adsorbates and the surface, and have been reported in the literature (all configurations studied are in Figures S1−S3).[31,36,37]

Surface Lattice Strain. An isotropic biaxial strain is applied to the surface plane only. Strain values range from +5% (tensile) to −5% (compressive) in intervals of 0.5%.

Surface Labeling. We use labels such as X%_{hkl}S-NH_2O−Y, where X% is the strain in percentage, {hkl} is the Miller index of the surface, S stands for stoichiometric, N is the water coverage, and Y is M for molecular and D for dissociative water.

Visualization and Imaging. Structures were visualized and drawn using VESTA.[38]

RESULTS AND DISCUSSION

The Energetics of Bare Surfaces. The surface energy γ_{Bare} was calculated from the energy of a stoichiometric surface $E_{Slab}^{Stoich,Bare}$, the energy of the unstrained bulk with the same number of CeO_2 units as the surface E_{Bulk,CeO_2}^{Stoich}, and the surface area A (2 is to account for the two symmetrical surfaces):

$$\gamma_{Bare} = \frac{E_{Slab}^{Stoich,Bare} - E_{Bulk,CeO_2}^{Stoich}}{2A} \quad (1)$$

The surface energy (eq 1) defines the stability of a surface, and the values for the unstrained {100}S, {110}S, and {111}S stoichiometric CeO_2 surfaces are in agreement with the

https://doi.org/10.1021/acs.jpcc.4c04172
J. Phys. Chem. C 2024, 128, 18451−18464

literature, with the order of stability following {111}S < {110}S < {100}S,[20,25,29−31] with {111} being the most stable, and {100} the least stable surfaces. Literature data for the surface energies are reported in Table 1.

Table 1. Surface Energy (J/m^2) of the Stoichiometric {100}, {110}, and {111} CeO_2 Surfaces Compared to Literature Values

methodology	{100}S (J/m^2)	{110}S (J/m^2)	{111}S (J/m^2)
this work PBE+U = 5 eV	1.45	1.06	0.70
PBE+U = 6 eV[39]	1.63		
PBE[20]	1.704		
PBE[20]		1.214	0.834
PBE+U = 5 eV	1.44	1.06	0.71
PBE+U = 5 eV[30]	1.41	1.05	0.67
PW91+U = 7 eV[25]		0.96	0.60
PW91+U = 5 eV[40]	1.65	1.39	0.68
PW91+U = 5 eV[41]	1.41	1.01	0.68
LDA[41,42]		1.35	1.04
PW91+U = 5 eV	1.41	1.04	0.69
LDA-PW91[43]		1.35	1.0
GGA-PW91[43]		1.05	0.7
HF[43]		2.11	1.31
PBE+U = 5 eV	1.45	1.06	0.70
PBE+U = 5 eV[26]	1.45	1.06	0.70
ML TU-TILD[a] [45]		1.19	0.78

[a]TU-TILD is combined with machine learning (ML) potentials and trained on results of ab initio molecular dynamics (AIMD).

The order of stability of strained and unstrained surfaces remains the same (Figure 1). Both tensile and compressive

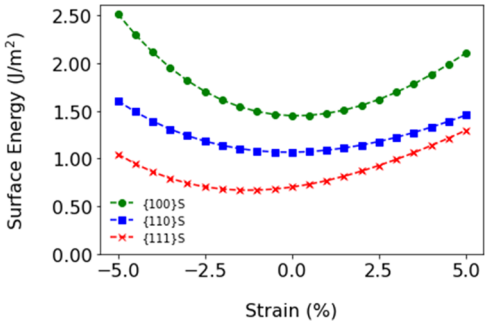

Figure 1. Surface energy of stoichiometric CeO_2 surfaces under compressive (negative) and tensile (positive) strains.

strain destabilize the surfaces, as they reduce and increase the length of Ce−O bonds, resulting in a weaker and stronger overlap of O 2p and Ce 5d/4f states, respectively.[46] It is interesting that the difference in surface energy between {110}S and {111}S decreases significantly as the tensile strain increases, while the difference in the energy among the three surfaces increases as compressive strain increases (Figure 1). Upon compressive strain between −2 and −0.5%, the surface energies of the strained {111} surface are lower than the unstrained {111} surface. However, these differences are relatively small of the order of 0.02−0.03 Jm^{2-}, which correspond to a 3−4.6% error on our energies. This effect is due to the small size of the {111} slab model used in this study with thickness of 5 surface layers.

The Energetics of Water Adsorption. The adsorption energy of water (eq 2) on stoichiometric surfaces is calculated from the energy of the stoichiometric surfaces with adsorbed water $E_{Slab}^{Stoich,Ads}$, the energy of a stoichiometric bare surface $E_{Slab}^{Stoich,Bare}$, and the energy of n_{H_2O} water molecules E_{H_2O} (where n = 1, 2, 3, 4 correspond to 25, 50, 75, and 100% water coverage on each side of the slab, and 2 is to account for the two symmetrical surfaces):

$$E_{Ads} = \frac{E_{Slab}^{Stoich,Ads} - (E_{Slab}^{Stoich,Bare} + 2n_{H_2O}E_{H_2O})}{2n_{H_2O}} \quad (2)$$

The adsorption energies for 25% water coverage of dissociative (−1.54 eV {100} > −1.06 eV {110} > −0.5 eV {111}), and molecular (−0.90 eV {100} > −0.77 eV {110} > −0.53 eV {111}) water adsorption on the stoichiometric surfaces are in line with the literature.[29,31,44,47] Literature data for the adsorption energies are reported in Table 2. Of note, the adsorption energies of the 0%_{111}S-25H_2O-M (−0.53 eV) and 0%_{111}S-25H_2O-D (−0.50 eV) compare well with the experimental values of (−)0.53 eV (at 0.2 ML) and (−)0.61 eV (unknown coverage) measured using temperature-programmed desorption (TPD) experiments.

The water adsorption on CeO_2 surfaces from 25% coverage to the monolayer adsorption as a function of compressive and tensile strain is presented in Figure 2A−F. Applied strain does not change the order of stability of adsorbed water on the stoichiometric surfaces. This is reflected in the hydrogen bonding network, which does not change drastically with strain (Figures S4−S5). Compressive strain destabilizes while tensile strain stabilizes water adsorption for all coverages of both the molecular and dissociative adsorptions. Increasing water coverage sees a destabilization of the dissociative water adsorption, which is also seen for the molecular adsorption of water on the {100} and {110} surfaces. Unlike the other surfaces, molecular adsorption is stabilized by an increase in water coverage for the {111} surface. However, the change in the adsorption energy of molecular water on the {111}S is quite small upon increasing coverage (0.02 eV from 25% to 100% water coverage), which is also supported by the literature.[29,49] Perhaps the most dramatic change is seen for the dissociative adsorption of water on the {111} surface, as under compressive strain the adsorption energy becomes positive, which is more pronounced as the water coverage increases.

Here, we only present the salient structural features of the water adsorption (Figure 2G−K), leaving detailed schematics of all adsorption geometries in Figures S1−S3. The adsorption configurations of dissociative water on the three surfaces of ceria do not change radically as a function of water coverage and strain. The same applies to the adsorption of molecular water on the {111} surface (Figure 2G). A reduced H bonding network would normally see a destabilization in the adsorption energy, but strain induces a reconstruction of the surface layers for the {110} surface, which is most likely the underlying cause of the large stabilization of the adsorption of molecular water on the {110} surface above 2.5% tensile strain (Figure 2H vs I). Although this reconstruction on the {110} surface occurs for all values of tensile strain, this appears to affect the adsorption of molecular water more, and to a lesser extent the adsorption of dissociative water. We also observe a breakdown in the adsorption trend for values of compressive strain below −0.5% for the adsorption of molecular water at 25% water coverage on the {100} surface. However, visual inspection reveals that this is

https://doi.org/10.1021/acs.jpcc.4c04172
J. Phys. Chem. C 2024, 128, 18451−18464

Table 2. Adsorption Energy of Water (eV) for Both Molecular and Dissociatively Adsorbed Water on Stoichiometric CeO_2 Surfaces at Different Coverages in H_2O/nm^2 and ML (Monolayer) in Brackets

surface label	methodology	adsorption energy (eV)	coverage H_2O/nm^2 (ML)
0%_{111}S-NH_2O-M[29]	PBE+U = 5 eV	−0.58/−0.56	1.28 (0.17)
0%_{111}S-NH_2O-M	this work, PBE+U = 5 eV	−0.53	1.90 (0.25)
0%_{111}S-NH_2O-M[48]	PW91+U = 5 eV	−0.35	- (0.25)
0%_{111}S-NH_2O-M[44]	PBE+U = 5 eV	−0.5	1.90 (0.25)
0%_{111}S-NH_2O-M[40]	PW91+U = 5 eV	−0.51	- (0.25)
0%_{111}S-NH_2O-M[49]	PBE	−0.49	- (0.25)
0%_{111}S-NH_2O-M	this work, PBE+U = 5 eV	−0.59	3.81 (0.5)
0%_{111}S-NH_2O-M[25]	PW91+U = 7 eV	−0.51	- (0.5)
0%_{111}S-NH_2O-M[29]	PBE+U = 5 eV	−0.60	3.83 (0.5)
0%_{111}S-NH_2O-M	this work, PBE+U = 5 eV	−0.56	7.64 (1)
0%_{111}S-NH_2O-M[29]	PBE+U = 5 eV	−0.57	7.67 (1)
0%_{111}S-NH_2O-D[31]	PBE+U = 5 eV	−0.6	1.27 (0.16)
0%_{111}S-NH_2O-D[29]	PBE+U = 5 eV	−0.59	1.28 (0.17)
0%_{111}S-NH_2O-D	this work, PBE+U = 5 eV	−0.50	1.90 (0.25)
0%_{111}S-NH_2O-D[50]	PBE+U = 5 eV	−0.57	- (0.25)
0%_{111}S-NH_2O-D[48]	PW91+U = 5 eV	−0.65	- (0.25)
0%_{111}S-NH_2O-D[44]	PBE+U = 5 eV	−0.5	1.90 (0.25)
0%_{111}S-NH_2O-D[49]	PBE	−0.65	- (0.25)
0%_{111}S-NH_2O-D[31]	PBE+U = 5 eV	−0.7	2.54 (0.33)
0%_{111}S-NH_2O-D	this work, PBE+U = 5 eV	−0.41	3.81 (0.5)
0%_{111}S-NH_2O-D[51]	PBE	−0.58	- (0.5)
0%_{111}S-NH_2O-D[31]	PBE+U = 5 eV	−0.58	3.81 (0.5)
0%_{111}S-NH_2O-D[31]	PBE+U = 5 eV	−0.56	5.09 (0.66)
0%_{111}S-NH_2O-D	this work, PBE+U = 5 eV	−0.13	7.64 (1)
0%_{111}S-NH_2O-D[29]	PBE+U = 5 eV	−0.15	7.67 (1)
0%_{111}S-NH_2O-D[51]	PBE	−0.55	- (1)
0%_{110}S-NH_2O-M	this work, PBE+U = 5 eV	−0.76	1.16 (0.25)
0%_{110}S-NH_2O-M[44]	PBE+U = 5 eV	−0.8	1.17 (0.25)
0%_{110}S-NH_2O-M[29]	PBE+U = 5 eV	−0.85	1.17 (0.25)
0%_{110}S-NH_2O-M	this work, PBE+U = 5 eV	−0.75	2.33 (0.5)
0%_{110}S-NH_2O-M[29]	PBE+U = 5 eV	−0.76	4.69 (0.5)
0%_{110}S-NH_2O-D	this work, PBE+U = 5 eV	−1.06	1.16 (0.25)
0%_{110}S-NH_2O-D[44]	PBE+U = 5 eV	−1	1.17 (0.25)
0%_{110}S-NH_2O-D[31]	PBE+U = 5 eV	−1.15	1.16 (0.25)
0%_{110}S-NH_2O-D[29]	PBE+U = 5 eV	−1.12	1.17 (0.25)
0%_{110}S-NH_2O-D	this work, PBE+U = 5 eV	−1.08	2.33 (0.5)
0%_{110}S-NH_2O-D[31]	PBE+U = 5 eV	−1.2	2.3 (0.5)
0%_{110}S-NH_2O-D	this work, PBE+U = 5 eV	−1.0	3.5 (0.75)
0%_{110}S-NH_2O-D[31]	PBE+U = 5 eV	−1.1	3.5 (0.75)
0%_{110}S-NH_2O-D[29]	PBE+U = 5 eV	−1.00	4.69 (0.5)
0%_{110}S-NH_2O-D	this work, PBE+U = 5 eV	−0.97	4.67 (1)
0%_{110}S-NH_2O-D[29]	PBE+U = 5 eV	−0.21	9.39 (1)
0%_{100}S-NH_2O-M	this work, PBE+U = 5 eV	−0.90	1.65 (0.25)
0%_{100}S-NH_2O-M[29]	PBE+U = 5 eV	−1.00	1.66 (0.25)
0%_{100}S-NH_2O-M[44]	PBE+U = 5 eV	−0.82	1.65 (0.25)
0%_{100}S-NH_2O-M	this work, PBE+U = 5 eV	−0.84	6.61 (1)
0%_{100}S-NH_2O-M[29]	PBE+U = 5 eV	−0.89	6.64 (1)
0%_{100}S-NH_2O-D	this work, PBE+U = 5 eV	−1.54	1.65 (0.25)
0%_{100}S-NH_2O-D[29]	PBE+U = 5 eV	−1.57	1.66 (0.25)
0%_{100}S-NH_2O-D[31]	PBE+U = 5 eV	−1.6	1.65 (0.25)
0%_{100}S-NH_2O-D[44]	PBE+U = 5 eV	−1.5	1.65 (0.25)
0%_{100}S-NH_2O-D	this work, PBE+U = 5 eV	−1.41	3.30 (0.5)
0%_{100}S-NH_2O-D[29]	PBE+U = 5 eV	−1.73/−0.87	3.32 (0.5)
0%_{100}S-NH_2O-D[31]	PBE+U = 5 eV	−1.3	3.5 (0.5)
0%_{100}S-NH_2O-D	this work, PBE+U = 5 eV	−1.46	4.96 (0.75)
0%_{100}S-NH_2O-D[31]	PBE+U = 5 eV	−1	4.96 (0.75)
0%_{100}S-NH_2O-D	this work, PBE+U = 5 eV	−1.42	6.61 (1)
0%_{100}S-NH_2O-D[29]	PBE+U = 5 eV	−0.89	6.64 (1)

not due to a surface restructuring, but a change in the adsorption configuration of molecular water molecules on the {100} surface (from flat to tilted, Figure 2J vs K) as reflected also in the hydrogen bonding network (Figure S4).

Temperature of Desorption. To compare the adsorption of water on the strained ceria surfaces, we calculate the temperature of desorption (T_D) using the approach implemented in Surfinpy.[52,53] This approach has been used successfully in previous studies.[29−31,44,54,55] T_D is the temperature at which water desorbs from the surface of ceria at a specific partial pressure of water, thus describing the phase boundary between two phases: the bare surface and the surface with adsorbed water.

https://doi.org/10.1021/acs.jpcc.4c04172
J. Phys. Chem. C 2024, 128, 18451−18464

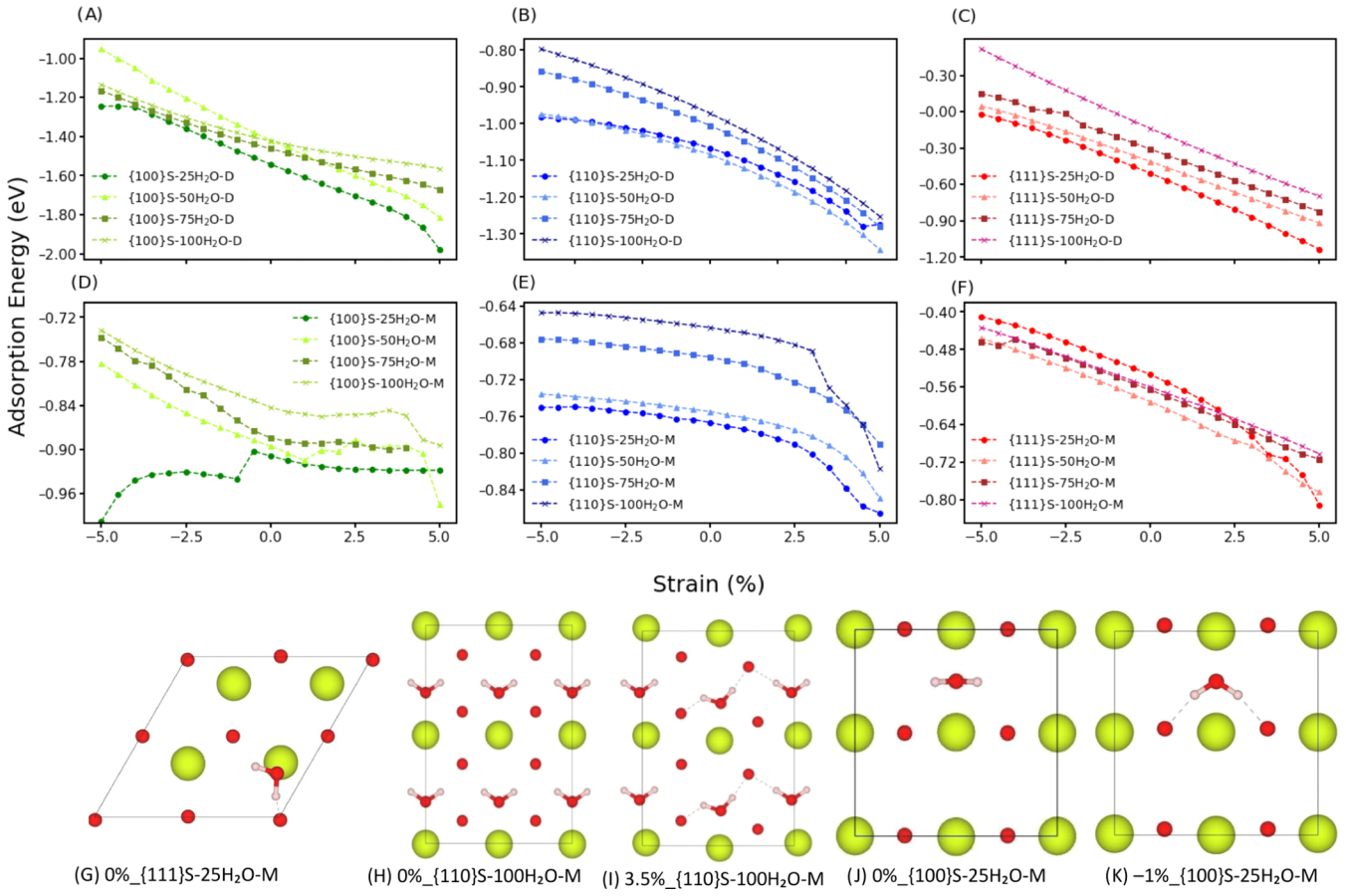

Figure 2. Adsorption energy of water on CeO_2 surfaces as a function of strain and water coverages (25−100%): dissociative water on the (A) {100}, (B) {110}, and (C) {111} surfaces, and molecular water on the (D) {100}, (E) {110}, and (F) {111} surfaces. The structure of adsorbed molecular water on (G) {111}, (H, I) {110}, and (J, K) {100} unstrained and strained surfaces.

The surface energy of surfaces with adsorbed water (eq 3) can be calculated from the surface energy of bare surfaces (eq 1), the water coverage $\left(\frac{n_{H_2O}}{2A}\right)$, the number of adsorbed water molecules n_{H_2O}, the surface area A, gas constant R, temperature T, and the partial pressures of water chosen p_{H_2O} and in the standard state p^o:

$$\gamma_{Ads} = \gamma_{Bare} + \frac{n_{H_2O}}{2A}\left(G_{Ads,(T)} - RT\ln\left(\frac{p_{H_2O}}{p^o}\right)\right) \quad (3)$$

where the adsorption energy of water as a function of temperature (eq 4) is

$$G_{Ads,(T)} = \frac{E_{Slab}^{Stoich,Ads} - (E_{Slab}^{Stoich,Bare} + 2n_{H_2O}G_{H_2O,(T)})}{2n_{H_2O}} \quad (4)$$

and the energy of water including temperature effects, $G_{H_2O,(T)}$ (eq 5), is calculated from the experimental entropy of gaseous water in the standard state $S_{(T)}$:[56]

$$G_{H_2O,(T)} = E_{H_2O} - TS_{(T)} \quad (5)$$

Future developments would benefit from calculating the vibrational frequency contributions of the solid phases ($E_{Slab}^{Stoich,Ads}$ and $E_{Slab}^{Stoich,Bare}$) to obtain a more accurate estimate of the free energy change. Our approach also does not include any kinetic effects due to the dissociation of water and this again should be in interesting topic to develop further.

Figures 3A and 4A map the desorption temperatures of dissociative and molecular adsorbed water on unstrained CeO_2 surfaces at different water coverage for selected partial pressures of water. Molecular water has a lower T_D than dissociative water, with water desorbing at lower temperature on the {111} followed by the {110} and the {100} surfaces at all partial pressures of water. T_D decreases with increasing coverage as the adsorption energy of water becomes less negative as coverage increases (Figure 2). This is in line with previous literature.[29,31]

Experimental measurements have revealed that a mixture of molecular and dissociative water can adsorb on the stoichiometric {111} and {100} surfaces of ceria.[57−64] Experimental data on the {110} CeO_2 surface is not available.

Little experimental data is available for the oxidized {100} CeO_2 surface, where water desorption has been shown to extend from near 200 K to beyond 500 K, with three peaks above 200, 300, and 400 K, on the {100} ceria surface indicating that water predominantly dissociated on this surface.[57] Our data for molecular and dissociatively adsorbed water shows temperatures of desorption in the range 222−238 and 356−393 K, respectively depending on coverage and assuming a partial pressure of 10^{-10} bar. The peak above 200 K is assigned to the presence of molecular adsorbed water, while the remaining peaks are related to strongly adsorbed hydroxyl groups.[57]

Most studies have been performed on the most stable {111} ceria surface. According to Temperature-Programmed Desorp-

https://doi.org/10.1021/acs.jpcc.4c04172
J. Phys. Chem. C 2024, 128, 18451−18464

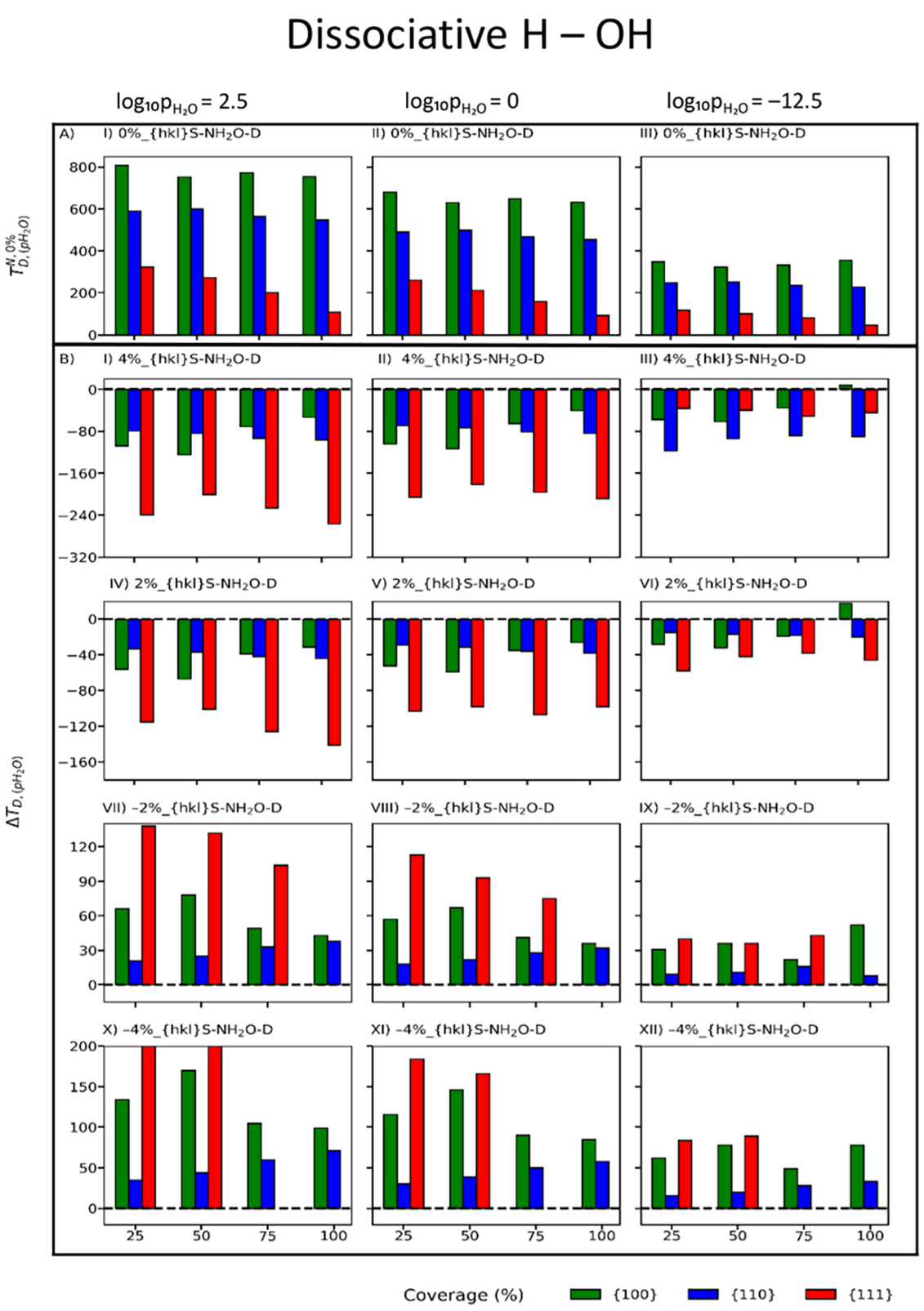

Figure 3. Temperature of desorption of dissociative (A) adsorbed water on the unstrained surfaces of CeO_2. Change in the temperature of desorption with respect to the unstrained surface ($\Delta T_{D,(pH_2O)}$) of dissociative (B) adsorbed water on the strained surfaces of CeO_2 at compressive (−4 and −2%) and tensile (4 and 2%) strains. Red, blue and green represent the {111}, {110}, and {100} CeO_2 surfaces, respectively.

tion (TPD) spectra, H_2O desorbs as a sharp feature around 200 K on the oxidized {111} ceria surface,[57,59−61] while hydroxyl groups mostly disappear below 250 K.[57−59,61] In the following text we have discussed relevant data where comparison could be done under certain assumptions.

A range of 170−185 K desorption temperatures (measured at 10^{-10} bar) was reported for the single water layer on the oxidized

https://doi.org/10.1021/acs.jpcc.4c04172
J. Phys. Chem. C 2024, 128, 18451−18464

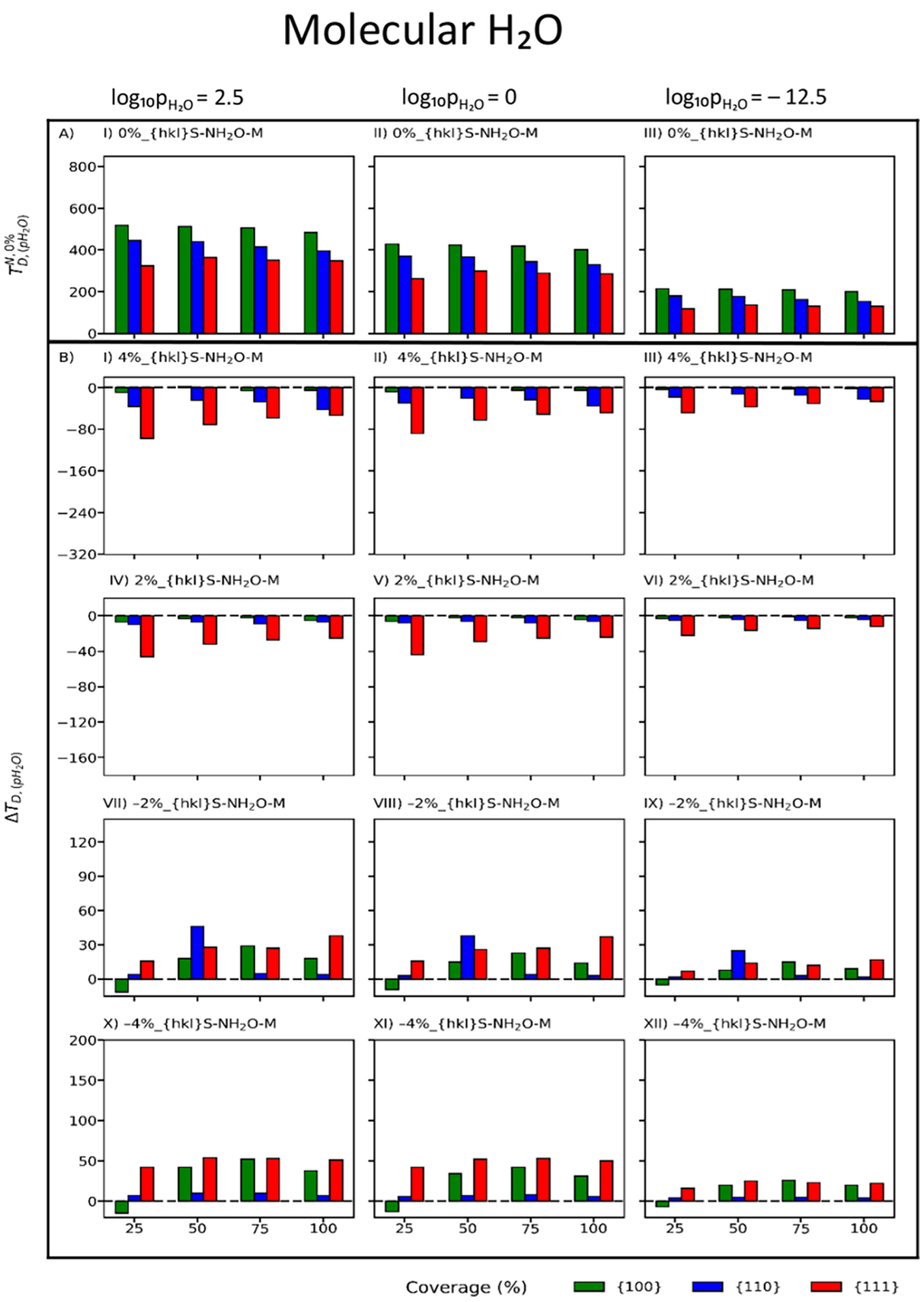

Figure 4. Temperature of desorption of molecular (A) adsorbed water on the unstrained surfaces of CeO_2. Change in the temperature of desorption with respect to the unstrained surface ($\Delta T_{D,(pH_2O)}$) of molecular (B) adsorbed water on the strained surfaces of CeO_2 at compressive (−4 and −2%) and tensile (4 and 2%) strains. Red, blue and green represent the {111}, {110}, and {100} CeO_2 surfaces, respectively.

{111} CeO_2 surface grown on the Cu(111) substrate, and a water desorption peak around 200 K (starting from 140−150 K) was measured at 10^{-10} bar on the oxidized {111} CeO_2 surface grown on Ru(0001).[58] Furthermore, D_2O was also found to desorb (using TDP at 10^{-10} bar) in three states with temperatures of 152, 200, and 275 K, representing respectively multilayer D_2O, weakly bound surface D_2O, and hydroxyl recombination.[63] These experimental values are higher than our

https://doi.org/10.1021/acs.jpcc.4c04172
J. Phys. Chem. C 2024, 128, 18451−18464

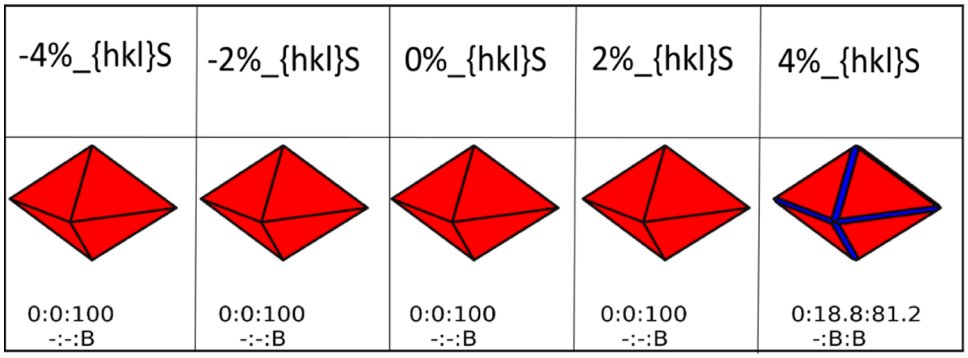

Figure 5. Shapes of CeO_2 bare nanoparticles. Red, blue and green represent the {111}, {110}, and {100} CeO_2 surfaces, respectively. The shapes of the nanoparticles are generated at a water partial pressure of 1 bar and 298 K. Each shape is characterized by a ratio of surfaces defined in numerical percentage ({100}:{110}:{111}). The label B defines a bare surface.

calculated temperature of 147 K for molecular water (at 10^{-10} bar) at the monolayer adsorption. In the range 130−200 K, a much higher concentration of molecular water was found compared to dissociatively adsorbed water,[58] which would support the computational finding that at the monolayer saturation molecularly adsorbed water has a much higher stability then dissociatively adsorbed water (Figure 2). However, experimentally chemisorbed water or multilayer/physisorbed water may coexist up to 150−170 K.[65]

Water desorption peaks were also measured in the range 195−320 K (at 10^{-12} bar) depending on water coverage on the oxidized {111} CeO_2 surface grown on the YSZ(111) substrate.[60] The 320 K is mostly the background adsorbed water (0.04−0.07 ML). As the water coverage is increased from 0.2 to 0.9 ML, the water desorption peak shifts from 265 to 200 K. This behavior was conceptualized considering the hydrogen bond network and water molecules being forced to reduce the number of hydrogen bonds to the surface when their concentration increases. The experimental values[60] are much higher than our calculated temperature of 119, 137, 131, 130 K for molecular water (at 10^{-12} bar) at 0.25, 0.5, 0.75, and 1 ML but much lower than 350 K at 0.25 ML calculated including the oxygen chemical potential.[49] We need to go to partial pressures of water of 10^{-5} bar to see temperature of desorption similar in magnitude to the experiments (171, 198, 190, and 188 K at 0.25, 0.5, 0.75, and 1 ML).

The discrepancies between the calculated and experimental temperatures of desorption are symptomatic of an experimental complexity that is yet to be considered in the calculations. However, considering the simple models used in the DFT calculations, these can provide some additional knowledge. Future studies should include mixed states of adsorbed water and surface structural features.

For each surface, the effect of strain can be better visualized as a change in desorption temperature (eq 6) with respect to the T_D of the unstrained $T^{N,0\%}_{D,(pH_2O)}$ and strained $T^{N,Strain\%}_{D,(pH_2O)}$ surface at a specific partial pressure (p_{H_2O}):

$$\Delta T_{D,(p_{H_2O})} = T^{N,0\%}_{D,(p_{H_2O})} - T^{N,strain\%}_{D,(p_{H_2O})} \quad (6)$$

A $\Delta T_{D,(p_{H_2O})} < 0$ indicates that the stability of the adsorption of water on strained surfaces is higher than that of unstrained surfaces, as $T^{N,Strain\%}_{D,(pH_2O)} > T^{N,0\%}_{D,(pH_2O)}$. The opposite occurs if $\Delta T_{D,(pH_2O)} > 0$. All temperatures of desorption for all configurations are provided in Figures S6−S7.

$\Delta T_{D,(pH_2O)}$ is much greater in magnitude for dissociatively than for molecularly adsorbed water. Irrespective of dissociative and molecular water adsorption, tensile strain sees negative changes ($\Delta T_{D,(pH_2O)} < 0$) in the desorption temperatures with a few exceptions (4%_{100}S-100H_2O-D, 2%_{100}S-100H_2O-D), and $\Delta T_{D,(pH_2O)}$ also becomes more negative as tensile strain increases (Figures 3B(I−VI) and 4B(I−VI)). Conversely, compressive strain sees positive changes ($\Delta T_{D,(pH_2O)} > 0$) in the desorption temperatures with a few exceptions (2%_{100}S-25H_2O-D, −2%_{100}S-25H_2O-D, −2%_{100}S-25H_2O-D, −4%_{100}S-25H_2O-D, −4%_{100}S-25H_2O-D, −4%_{100}S-25H_2O-D), and $\Delta T_{D,(pH_2O)}$ also becomes more positive as compressive strain increases (Figures 3B(VII−XII) and 4B(VII−XII)). Finally, on strained surfaces, as the partial pressure of water decreases, $\Delta T_{D,(pH_2O)}$ becomes less negative and less positive for tensile and compressive strains, respectively.

Morphology of Strained Cerium Dioxide Nanoobjects. The prediction of the shape of nanoobjects, either nanoparticles or nanograins, is important as it will define the thermodynamic shape of the constituents of the material. If the nanoobject is a nanoparticle, then this can be grown on a substrate or be part of a core@shell structure, where the mismatch between the lattices of the different materials will define the strain imposed on the nanoparticle and thus its thermodynamic morphology. If the nanoobject is a nanograin, then this would be part of a poly nanocrystalline material and, as such, be strained by other differently oriented nanograins of the same material or of different materials in composites.

The shape of ceria nanoobjects as a function of strain, temperature and partial pressure are generated using the Wulff construction[66−68] and follow a well-established methodology.[30,31] To generate the morphologies, the surface area phase diagrams representing surface composition alongside the ratio of the three surfaces are also needed and presented in the Supporting Information (Figures S8−S13). For each morphology presented in Figures 4 and 5, we also report the ratio of the surfaces expressed by the nanoparticle, i.e., {100}:{110}:{111}. It is this ratio determines the nanoparticle morphology. Each surface expressed by the nanoobject also has a different composition as it could be hydrated or bare depending on the external conditions.

When we only consider bare surfaces (Figure 5), the {111} surface dominates all morphologies for CeNPs, at any compressive and tensile strain.

https://doi.org/10.1021/acs.jpcc.4c04172
J. Phys. Chem. C 2024, 128, 18451−18464

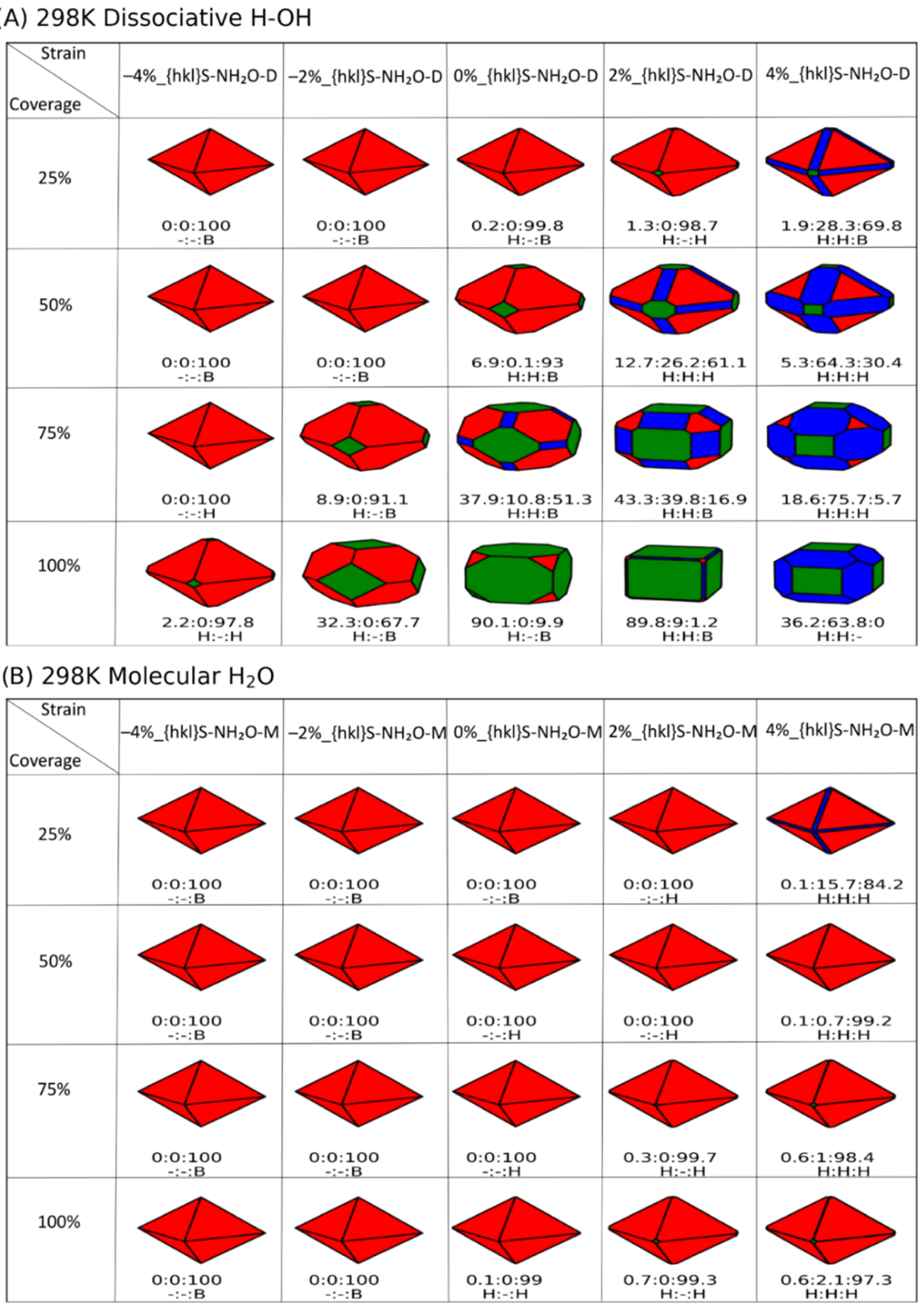

Figure 6. Shapes of CeO_2 nanoparticles in the presence of dissociative (A) and molecular (B) water. Red, blue and green represent the {111}, {110}, and {100} CeO_2 surfaces, respectively. The shapes of the nanoparticles are generated at a water partial pressure of 1 bar and 298 K. Each shape is characterized by a ratio of surfaces defined in numerical percentage ({100}:{110}:{111}). There is also a set of labels, H (hydrated surface) and B (bare surface), which determine whether the corresponding surface has water adsorbed on it or not.

For dissociative water adsorption (Figure 6A), increasing water coverage at constant strain primarily stabilizes the {100} and {110} surfaces, particularly for tensile strain: the octahedral shape leads the way to the formation of truncated octahedral, cuboidal, and truncated cuboidal morphologies at higher water coverage and strain. Under standard temperature and pressure conditions, at all strains the {110} and {100} surfaces are

https://doi.org/10.1021/acs.jpcc.4c04172
J. Phys. Chem. C 2024, 128, 18451−18464

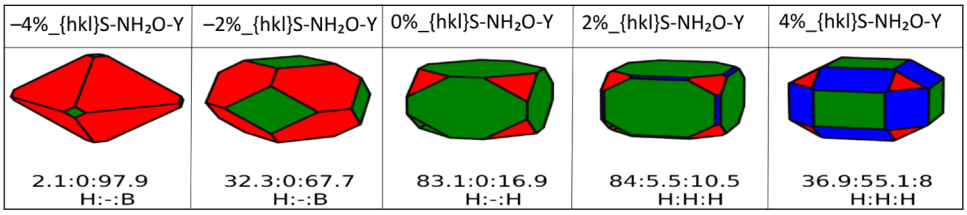

Figure 7. Shapes of CeO_2 nanoparticles at 298 K and 1 bar partial pressure of water, considering only the most stable phases within a constant value of strain, at all water coverages and independently on the dissociative or molecular water adsorption. Each shape is characterized by a ratio of surfaces defined in numerical percentage ({100}:{110}:{111}). There is also a set of labels, H (hydrated surface) and B (bare surface), which determine whether the corresponding surface has water adsorbed on it or not. Red, blue and green represent the {111}, {110}, and {100} CeO_2 surfaces, respectively.

hydrated, while the {111} surface transitions between hydrated and bare at higher strain depending on higher water coverage.

For molecularly adsorbed water (Figure 6B), an octahedral nanoobject expressing the {111} surface is the predominant morphology for all water coverages for all strain values. There is minimal appearance of the {110} surface as an edge and the {100} surface as a truncated corner, under tensile strain and it is more accentuated at lower water coverage. Under standard temperature and pressure conditions, at all strains the {110} and {100} surfaces are hydrated, whereas unlike compressive strain, tensile strain stabilizes the hydration of the {111} surfaces. As the temperature increases from 298 to 673 K (Figures S14−S17), we see an increase in the {110} surface in the morphology of CeNPs when molecular water is adsorbed, but this is not sufficient to significantly deform the octahedral shape of the nanoparticles. When water is adsorbed dissociatively, and temperature is increased, we observed the opposite behavior with the disappearance of the {110} and {100} surfaces (which would otherwise stabilize truncated octahedral morphologies), while the {111} surface becomes predominant, favoring a more pristine octahedral shape.

For completeness, we have generated morphologies at 298 K and 1 bar partial pressure of water (Figure 7), considering only the most stable phases within a constant value of strain, at all water coverages and independently on the dissociative or molecular water adsorption (i.e., X%_{100}S-100H_2O-D, X%_{110}S-100H_2O-D, and X%_{111}S-100H_2O-M). These nanoparticles are similar to the shapes of those constructed using only surfaces adsorbed with dissociative water molecules at the monolayer adsorption (100% water coverage, Figure 6A).

Controlling the shape of nanoparticles is important to tune catalytic activity. Cuboidal NPs mostly expressing the {100} surface[69] display enhanced CO catalytic oxidation compared with truncated octahedral NPs exposing both the {111} and {100} surfaces.[70] As water facilitates the CO oxidation process,[71] tensile strain and a full monolayer of water would be needed to stabilize cuboidal nanoceria as shown in Figure 6A.

Experimentally, many factors have been shown to affect the shape of nanoceria, including the concentration of alkaline solutions,[72] the presence of precipitating agents,[73] capping agents,[74] the solution pH,[75] the synthesis temperature[76,77] and time,[78] and thermal aging.[79] Strain is another factor but is as of yet less explored since it is more complicated to control this experimentally. Computationally, of course, this is not the case so modeling can be used as an explorative tool.

The use of strain to tune the morphology of nanoparticles is indeed less common,[80,81] with few studies on ceria NPs. Imposing an intrinsic surface strain by crossing the nanoscale can be an effective strategy to regulate catalytic (nanozymatic) activity. This has been shown in ultrathin ∼1.2 nm CeO_2 nanoplates that experience an intrinsic surface tensile strain (3.0% in plane/10.0% out of plane), which ultimately induces a tetragonal distortion and an increase in the covalency of the Ce−O bonds, leading to a ∼2.6-fold increase in superoxide dismutase (SOD) mimetic activity compared with unstrained ceria nanoparticles.[12] Although, our results did not display nanoplates, this would depend on synthesis conditions and there will be kinetic effects that we cannot yet simulate. Whereas phase transitions are known to occur in CeNPs under strain,[82] voids of geometrical shapes,[83,84] and faceting[85,86] have still to be related to the presence of localized surface strain.

Lattice mismatch induced strain is at the core of core@shell structures and supported films. Whereas lattice strain can be easily calculated in supported films, it is more complicated when it comes to core−shell structures. Crystalline supported nanofilms CeO_2(100)/STO(001) and CeO_2(100)/YSZ(001) experience tensile (2.1%) and compressive (−5.6%) strains respectively, which are linked to an increase in the concentrations of Ce^{3+} (up to 4-fold).[14] On the other hand, a precise measure of the strain exerted by the lattice mismatch in core@shell nanostructures is difficult because of the curvature of the nanoobject, which makes it even more complicated to evaluate the effect of strain on the exerted activity.

However, it is also complicated to decouple the intricate interplay established between the lattice mismatch (and thus strain) strain and the nature of the interaction between the different materials in the core@shell structures, and whether these interactions may enhance activity of such nanostructures. Although there is no information on the strain exerted by the different materials, there are some examples to cite where core@shell structures can improve the photocatalytic reduction of CO_2 (spherical CdS@CeO_2),[87] the photocatalytic water splitting (rod-like TiO_2@CeO_2),[88] and the chemoselective reduction of nitro compounds (spherical AgNP@CeO_2).[89]

CONCLUSIONS

We have demonstrated that modeling based on density functional theory can aid the interpretation of strain effects in nanoceria. By evaluating the adsorption free energies for water adsorbed on strained surfaces of ceria, we can implement a thermodynamic strategy to evaluate the morphology of particles (whether present as nanoparticles or nanograins) as a function of variables, such as temperature and partial pressure of water, that can be controlled experimentally.

Independent of tensile or compressive strain applied to the surface, the stability of low Miller index surfaces follows {111} > {110} > {100}, which is the same as unstrained surfaces. Compressive strain destabilizes the adsorption of water at

https://doi.org/10.1021/acs.jpcc.4c04172
J. Phys. Chem. C 2024, 128, 18451−18464

different coverages, while tensile strain stabilizes it. We see drastic stabilization effects when the {110} surface structure restructures significantly under tensile strain.

The thermodynamic strategy implemented can aid the evaluation of the temperature of desorption of water on strained surfaces. We see that tensile strain increases the temperature of desorption while compressive strain has the opposite effect. We found that there is a thermodynamic driving force toward octahedral morphologies under all strains when molecular water is adsorbed on the surfaces of nanoceria. However, at high partial pressure of water and tensile strains, cuboidal nanoceria can be stabilized, if dissociative water is present at its surfaces.

Our atomistic modeling has allowed us to quantify strain effects related to nanoceria and its interaction with molecular and dissociative water. As we have only considered cases where water is separately adsorbed molecularly and dissociatively, future research should develop toward more complicated mixed phases. Such an approach can be used widely for the prediction of strained particle morphologies of materials and minerals in relevant environmental conditions.

■ ASSOCIATED CONTENT

Data Availability Statement

Raw data are available at https://doi.org/10.17632/3hwx68h2ny.

Supporting Information

The Supporting Information is available free of charge at https://pubs.acs.org/doi/10.1021/acs.jpcc.4c04172.

Adsorption configurations of water on strained ceria surfaces (Figures S1−S3), the hydrogen bond network between adsorbed water and ceria surfaces (Figures S4−S5), temperature of desorption of water on ceria surfaces (Figures S6−S7), "surface area" phase diagrams (Figures S8−S13), and predicted ceria particle morphology (Figures S14−S17) (PDF)

■ AUTHOR INFORMATION

Corresponding Authors

Sidra Munir − *Department of Physical and Life Sciences, University of Huddersfield, Huddersfield HD1 3DH, U.K.*; Email: sidra.munir@hud.ac.uk

Marco Molinari − *Department of Physical and Life Sciences, University of Huddersfield, Huddersfield HD1 3DH, U.K.*; orcid.org/0000-0001-7144-6075; Email: m.molinari@hud.ac.uk

Authors

Khoa Minh Ta − *Department of Physical and Life Sciences, University of Huddersfield, Huddersfield HD1 3DH, U.K.*

Thomas Smith − *Department of Physical and Life Sciences, University of Huddersfield, Huddersfield HD1 3DH, U.K.*; orcid.org/0000-0002-9956-4046

Lisa J. Gillie − *Department of Physical and Life Sciences, University of Huddersfield, Huddersfield HD1 3DH, U.K.*; orcid.org/0000-0003-4423-7387

David J. Cooke − *Department of Physical and Life Sciences, University of Huddersfield, Huddersfield HD1 3DH, U.K.*; orcid.org/0000-0001-5996-7900

Stephen C. Parker − *Department of Chemistry, University of Bath, Bath BA2 7AY, U.K.*; orcid.org/0000-0003-3804-0975

Complete contact information is available at: https://pubs.acs.org/10.1021/acs.jpcc.4c04172

Author Contributions

S.M., K.M.T., T.S., and M.M.: formal analysis, investigation, visualization, and writing—original draft. M.M., D.J.C., L.J.G., and S.C.P.: conceptualization, methodology, validation, resources, and data curation. M.M., D.J.C., and L.J.G.: supervision, project administration, and funding acquisition. S.M., K.M.T., T.S., D.J.C., L.J.G., S.C.P., and M.M.: writing—review and editing.

Notes

The authors declare no competing financial interest.

■ ACKNOWLEDGMENTS

Calculations were run on the ARCHER2 UK National Supercomputing Services via our membership of the UK HEC Materials Chemistry Consortium (HEC MCC) funded by the EPSRC (EP/R029431/1, EP/X035859/1). Analysis was performed on the Orion computing facility and the Violeta HPC at the University of Huddersfield. K.M.T. is funded via the Vice Chancellor's Scholarship Scheme at the University of Huddersfield. T.S. is funded by EPSRC-DTP 2018-19 University of Huddersfield (EP/R513234/1).

■ REFERENCES

(1) Montini, T.; Melchionna, M.; Monai, M.; Fornasiero, P. Fundamentals and Catalytic Applications of CeO_2-Based Materials. *Chem. Rev.* **2016**, *116*, 5987−6041.

(2) Ahn, S.-Y.; Jang, W.-J.; Shim, J.-O.; Jeon, B.-H.; Roh, H.-S. CeO_2-Based Oxygen Storage Capacity Materials In Environmental And Energy Catalysis For Carbon Neutrality: Extended Application And Key Catalytic Properties. *Catal. Rev.* **2023**, *63*, 1−84.

(3) Wei, F.; Neal, C. J.; Sakthivel, T. S.; Fu, Y.; Omer, M.; Adhikary, A.; Ward, S.; Ta, K. M.; Moxon, S.; Molinari, M.; et al. A Novel Approach for the Prevention of Ionizing Radiation-Induced Bone Loss Using a Designer Multifunctional Cerium Oxide Nanozyme. *Bioact. Mater.* **2023**, *21*, 547−565.

(4) Pugazhendhi, A. S.; Neal, C. J.; Ta, K. M.; Molinari, M.; Kumar, U.; Wei, F.; Kolanthai, E.; Ady, A.; Drake, C.; Hughes, M.; et al. A Neoteric Antibacterial Ceria-Silver Nanozyme for Abiotic Surfaces. *Biomaterials* **2024**, *307*, No. 122527.

(5) Yang, X.; Wang, Y.; Tong, X.; Yang, N. Strain Engineering in Electrocatalysts: Fundamentals, Progress, and Perspectives. *Adv. Eng. Mater.* **2022**, *12*, No. 2102261.

(6) Schweiger, S.; Kubicek, M.; Messerschmitt, F.; Murer, C.; Rupp, J. L. A Microdot Multilayer Oxide Device: Let Us Tune the Strain-Ionic Transport Interaction. *ACS Nano* **2014**, *8*, 5032−5048.

(7) Pergolesi, D.; Fabbri, E.; Cook, S. N.; Roddatis, V.; Traversa, E.; Kilner, J. A. Tensile Lattice Distortion Does not affect Oxygen Transport In Yttria-Stabilized Zirconia−CeO_2 Heterointerfaces. *ACS Nano* **2012**, *6*, 10524−10534.

(8) Harrington, G. F.; Kim, S.; Sasaki, K.; Tuller, H. L.; Grieshammer, S. Strain-Modified Ionic Conductivity In Rare-Earth Substituted Ceria: Effects of Migration Direction, Barriers, and Defect-Interactions. *J. Mater. Chem. A* **2021**, *9*, 8630−8643.

(9) Rehman, S.; Kim, H.; Patil, H.; Kadam, K. D.; Sagar, R. U. R.; Aziz, J.; Um, D. S.; Khan, M. F.; Kim, D.-k. Current Rectification, Resistive Switching, and Stable NDR Effect in $BaTiO_3/CeO_2$ Heterostructure Devices. *Adv. Electron. Mater.* **2021**, *7*, No. 2001237.

(10) Guo, Z.; Kang, X.; Zheng, X.; Huang, J.; Chen, S. PdCu Alloy Nanoparticles Supported on CeO_2 Nanorods: Enhanced Electrocatalytic Activity by Synergy of Compressive Strain, Pdo and Oxygen Vacancy. *J. Catal.* **2019**, *374*, 101−109.

(11) Han, S. I.; Lee, S.-w.; Cho, M. G.; Yoo, J. M.; Oh, M. H.; Jeong, B.; Kim, D.; Park, O. K.; Kim, J.; Namkoong, E.; et al. Epitaxially

Strained CeO_2/Mn_3O_4 Nanocrystals as an Enhanced Antioxidant for Radioprotection. *Adv. Mater.* **2020**, *32*, No. 2001566.
(12) Liu, C.; Gui, L.; Zheng, J.-J.; Xu, Y.-Q.; Song, B.; Yi, L.; Jia, Y.; Taledaohan, A.; Wang, Y.; Gao, X.; et al. Intrinsic Strain-Mediated Ultrathin Ceria Nanoantioxidant. *J. Am. Chem. Soc.* **2023**, *145*, 19086−19097.
(13) Sayle, D. C.; Caddeo, F.; Morgan, L. M.; Neale, R. L.; Sayle, T. X. T.; Brambila, C.; Nutter, J.; Bhatta, U.; Ta, K. M.; Flitcroft, J. M.; et al. Aging Mechanisms Of Nanoceria And Pathways For Preserving Optimum Morphology. *Nano Today* **2023**, *51*, No. 101916.
(14) Balaji Gopal, C.; García-Melchor, M.; Lee, S. C.; Shi, Y.; Shavorskiy, A.; Monti, M.; Guan, Z.; Sinclair, R.; Bluhm, H.; Vojvodic, A.; Chueh, W. C. Equilibrium Oxygen Storage Capacity of Ultrathin $CeO_{2-\delta}$ Depends Non-Monotonically on Large Biaxial Strain. *Nat.Commun.* **2017**, *8*, No. 15360.
(15) Rong, W.; Chen, H.; Huang, Z.; Wu, K. Strain-Induced Oxygen Vacancies in Monolayered CeO_2(111) Islands Grown on Pt(111). *J. Phys. Chem. C* **2020**, *124*, 6284−6289.
(16) Castellarin-Cudia, C.; Surnev, S.; Schneider, G.; Podlucky, R.; Ramsey, M.; Netzer, F. Strain-Induced Formation of Arrays of Catalytically Active Sites at the Metal−Oxide Interface. *Surf. Sci.* **2004**, *554*, L120−L126.
(17) Zhang, L.; Sun, L.; Meng, Q.; Wu, J.; Hao, X.; Zhai, S.; Dou, W.; Jia, Y.; Zhou, M. Strain-Engineered Formation, Migration, and Electronic Properties of Polaronic Defects in CeO_2. *Phys. Status Solidi B* **2021**, *258*, No. 2100020.
(18) Aidhy, D. S.; Liu, B.; Zhang, Y.; Weber, W. J. Strain-Induced Phase and Oxygen-Vacancy Stability in Ionic Interfaces from First-Principles Calculations. *J. Phys. Chem. C* **2014**, *118*, 30139−30144.
(19) Kildgaard, J. V.; Hansen, H. A.; Vegge, T. DFT+ U Study of Strain-Engineered CO_2 Reduction on a CeO_{2-x} (111) Facet. *J. Phys. Chem. C* **2021**, *125*, 14221−14227.
(20) Liu, Z.; Wang, B.; Cazorla, C. Mechanical And Electronic Properties of CeO_2 Under Uniaxial Tensile Loading: A DFT Study. *Materialia* **2021**, *15*, No. 101050.
(21) Liu, Z.; Menéndez, C.; Shenoy, J.; Hart, J. N.; Sorrell, C. C.; Cazorla, C. Strain Engineering Of Oxide Thin Films for Photocatalytic Applications. *Nano Energy* **2020**, *72*, No. 104732.
(22) Ansari, S. A.; Khan, M. M.; Ansari, M. O.; Kalathil, S.; Lee, J.; Cho, M. H. Band Gap Engineering of CeO_2 Nanostructure Using an Electrochemically Active Biofilm For Visible Light Applications. *RSC Adv.* **2014**, *4*, 16782−16791.
(23) Wu, T.; Vegge, T.; Hansen, H. A. Improved Electrocatalytic Water Splitting Reaction on CeO_2(111) by Strain Engineering: A DFT +U Study. *ACS Catal.* **2019**, *9*, 4853−4861.
(24) Fan, J.; Xu, B.; Zhao, J.; Xu, H. Controllable Dissociation Of H_2O on a CeO_2(111) Surface. *Phys. Chem. Chem. Phys.* **2018**, *20*, 1575−1582.
(25) Chen, H. T.; Choi, Y. M.; Liu, M.; Lin, M.-C. A Theoretical Study of Surface Reduction Mechanisms of CeO_2 (111) and (110) by H_2. *ChemPhysChem* **2007**, *8*, 849−855.
(26) Ta, K. M.; Cooke, D. J.; Gillie, L. J.; Parker, S. C.; Seal, S.; Wilson, P. B.; Phillips, R. M.; Skelton, J. M.; Molinari, M. Infrared and Raman Diagnostic Modeling of Phosphate Adsorption on Ceria Nanoparticles. *J. Phys. Chem. C* **2023**, *127*, 20183−20193.
(27) Kresse, G.; Furthmüller, J. Efficiency Of Ab-Initio Total Energy Calculations for Metals and Semiconductors Using A Plane-Wave Basis Set. *Comput. Mater. Sci.* **1996**, *6*, 15−50.
(28) Dudarev, S. L.; Botton, G. A.; Savrasov, S. Y.; Humphreys, C.; Sutton, A. P. Electron-Energy-Loss Spectra and the Structural Stability of Nickel Oxide: An LSDA+ U Study. *Phys. Rev. B* **1998**, *57*, 1505.
(29) Molinari, M.; Parker, S. C.; Sayle, D. C.; Islam, M. S. Water Adsorption and Its Effect on the Stability of Low Index Stoichiometric and Reduced Surfaces of Ceria. *J. Phys. Chem. C* **2012**, *116*, 7073−7082.
(30) Symington, A. R.; Harker, R. M.; Storr, M. T.; Molinari, M.; Parker, S. C. Thermodynamic Evolution of Cerium Oxide Nanoparticle Morphology Using Carbon Dioxide. *J. Phys. Chem. C* **2020**, *124*, 23210−23220.
(31) Symington, A. R.; Molinari, M.; Moxon, S.; Flitcroft, J. M.; Sayle, D. C.; Parker, S. C. Strongly Bound Surface Water affects the Shape Evolution of Cerium Oxide Nanoparticles. *J. Phys. Chem. C* **2020**, *124*, 3577−3588.
(32) Smith, T.; Moxon, S.; Tse, J.; Skelton, J.; Cooke, D.; Gillie, L.; da Silva, E. L.; Silva, E.; Harker, R.; Storr, M.; Parker, S. Structural Dynamics Of Schottky And Frenkel Defects In CeO_2: A Density-Functional Theory Study. *J. Phys.: Energy* **2023**, *5*, No. 025004.
(33) Anwar, N.; Harker, R. M.; Storr, M. T.; Molinari, M.; Skylaris, C.-K. Linear-scaling density functional theory (DFT) simulations of point, Frenkel and Schottky defects in CeO_2. *Comput. Mater. Sci.* **2023**, *229*, No. 112396.
(34) Molinari, M.; Symington, A. R.; Sayle, D. C.; Sakthivel, T. S.; Seal, S.; Parker, S. C. Computer-Aided Design of Nanoceria Structures as Enzyme Mimetic Agents: The Role of Bodily Electrolytes on Maximizing Their Activity. *ACS Appl. Bio Mater.* **2019**, *2*, 1098−1106.
(35) Watson, G. W.; Kelsey, E. T.; de Leeuw, N. H.; Harris, D. J.; Parker, S. C. Atomistic Simulation Of Dislocations, Surfaces And Interfaces In MgO. *J. Chem. Soc., Faraday Trans.* **1996**, *92*, 433−438.
(36) Tegner, B. E.; Molinari, M.; Kerridge, A.; Parker, S. C.; Kaltsoyannis, N. Water Adsorption on AnO_2 {111}, {110}, and {100} Surfaces (An = U and Pu): A Density Functional Theory + U Study. *J. Phys. Chem. C* **2017**, *121*, 1675−1682.
(37) Moxon, S.; Symington, A. R.; Joshua, S. T.; Dawson, J.; Flitcroft, J. M.; Parker, S. C.; Cooke, D. J.; Harker, R. M.; Molinari, M. The Energetics Of Carbonated PuO_2 Surfaces affects Nanoparticle Morphology: A DFT+U Study. *Phys. Chem. Chem. Phys.* **2020**, *22*, 7728−7737.
(38) Momma, K.; Izumi, F. Vesta3 For Three-Dimensional Visualization Of Crystal, Volumetric And Morphology Data. *J. Appl. Crystallogr.* **2011**, *44*, 1272−1276.
(39) Chen, Y.; Lv, S.; Chen, C.; Qiu, C.; Fan, X.; Wang, Z. Controllable Synthesis of Ceria Nanoparticles with Uniform Reactive {100} Exposure Planes. *J. Phys. Chem. C* **2014**, *118*, 4437−4443.
(40) Marrocchelli, D.; Yildiz, B. First-Principles Assessment of H_2S and H_2O Reaction Mechanisms and the Subsequent Hydrogen Absorption on the CeO_2(111) Surface. *J. Phys. Chem. C* **2012**, *116*, 2411−2424.
(41) Nolan, M.; Grigoleit, S.; Sayle, D. C.; Parker, S. C.; Watson, G. W. Density Functional Theory Studies Of The Structure And Electronic Structure Of Pure And Defective Low Index Surfaces Of Ceria. *Surf. Sci.* **2005**, *576*, 217−229.
(42) Nolan, M.; Parker, S. C.; Watson, G. W. The Electronic Structure Of Oxygen Vacancy Defects At The Low Index Surfaces Of Ceria. *Surf. Sci.* **2005**, *595*, 223−232.
(43) Skorodumova, N. V.; Baudin, M.; Hermansson, K. Surface Properties of CeO_2 from First Principles. *Phys. Rev. B* **2004**, *69*, No. 075401.
(44) Moxon, S.; Symington, A.; Tse, J.; Flitcroft, J.; Skelton, J.; Gillie, L.; Cooke, D.; Parker, S.; Molinari, M. Composition-Dependent Morphologies of CeO_2 Nanoparticles in the Presence of Co-Adsorbed H_2O and CO_2: A Density Functional Theory Study. *Nanoscale* **2024**, *16*, 11232−11249.
(45) Kholtobina, A. S.; Forslund, A.; Ruban, A. V.; Johansson, B.; Skorodumova, N. V. Temperature Dependence of (111) and (110) Ceria Surface Energy. *Phys. Rev. B* **2023**, *107*, No. 035407.
(46) Ma, D.; Lu, Z.; Tang, Y.; Li, T.; Tang, Z.; Yang, Z. Effect Of Lattice Strain on the Oxygen Vacancy Formation and Hydrogen Adsorption at CeO_2(111) Surface. *Phys. Lett. A* **2014**, *378*, 2570−2575.
(47) Ma, Y.; Tian, Z.; Zhai, W.; Qu, Y. Insights On Catalytic Mechanism of CeO_2 as Multiple Nanozymes. *Nano Res.* **2022**, *15*, 10328−10342.
(48) Watkins, M. B.; Foster, A. S.; Shluger, A. L. Hydrogen Cycle on CeO_2 (111) Surfaces: Density Functional Theory Calculations. *J. Phys. Chem. C* **2007**, *111*, 15337−15341.
(49) Fronzi, M.; Piccinin, S.; Delley, B.; Traversa, E.; Stampfl, C. Water Adsorption on the Stoichiometric and Reduced CeO_2 (111) Surface: A First-Principles Investigation. *Phys. Chem. Chem. Phys.* **2009**, *11*, 9188−9199.

https://doi.org/10.1021/acs.jpcc.4c04172
J. Phys. Chem. C 2024, 128, 18451−18464

(50) Yang, Z.; Wang, Q.; Wei, S.; Ma, D.; Sun, Q. The Effect of Environment on the Reaction of Water on the Ceria(111) Surface: A DFT+U Study. *J. Phys. Chem. C* **2010**, *114*, 14891−14899.
(51) Kumar, S.; Schelling, P. K. Density Functional Theory Study Of Water Adsorption At Reduced And Stoichiometric Ceria (111) Surfaces. *J. Chem. Phys.* **2006**, *125*, No. 204704.
(52) Symington, A. R.; Tse, J.; Molinari, M.; Marmier, A.; Parker, S. surfinpy: A Surface Phase Diagram Generator. *J. Open Source Software* **2019**, *4*, 1210 DOI: 10.21105/joss.01210.
(53) Tse, J. S.; Molinari, M.; Parker, S. C.; Symington, A. R. SurfinPy 2.0: A Phase Diagram Generator for Surfaces and Bulk Phases. *J. Open Source Software* **2022**, *7*, 4014.
(54) Moxon, S.; Flitcroft, J. M.; Gillie, L. J.; Cooke, D. J.; Skelton, J. M.; Parker, S. C.; Molinari, M. Composition-Dependent Morphology Of Stoichiometric And Oxygen Deficient PuO_2 Nanoparticles In The Presence Of H_2O And CO_2: A Density-Functional Theory Study. *Appl. Surf. Sci.* **2024**, *676*, No. 160997.
(55) Tse, J. S.; Grant, J.; Skelton, J. M.; Gillie, L. J.; Zhu, R.; Pesce, G. L.; Ball, R. J.; Parker, S. C.; Molinari, M. Location of Artinite ($Mg_2CO_3(OH)_2{\cdot}3H_2O$) within the $MgO-CO_2-H_2O$ system using ab initio thermodynamics. *Phys. Chem. Chem. Phys.* **2023**, *25*, 18011−18022.
(56) Chase, M. W.; Organization, N. I. S.. *NIST-JANAF Thermochemical Tables.*; American Chemical Society: Washington, DC, 1998; Vol. *9*.
(57) Mullins, D. R.; Albrecht, P. M.; Chen, T.-L.; Calaza, F. C.; Biegalski, M. D.; Christen, H. M.; Overbury, S. H. Water Dissociation on $CeO_2(100)$ and $CeO_2(111)$ Thin Films. *J. Phys. Chem. C* **2012**, *116*, 19419−19428.
(58) Matolín, V.; Matolínová, I.; Dvořák, F.; Johánek, V.; Mysliveček, J.; Prince, K. C.; Skála, T.; Stetsovych, O.; Tsud, N.; Václavů, M.; Šmíd, B. Water Interaction with $CeO_2(111)/Cu(111)$ Model Catalyst Surface. *Catal. Today* **2012**, *181*, 124−132.
(59) Kundakovic, L.; Mullins, D. R.; Overbury, S. H. Adsorption and Reaction of H_2O and CO on Oxidized and Reduced Rh/CeOx(111) surfaces. *Surf. Sci.* **2000**, *457*, 51−62.
(60) Henderson, M. A.; Perkins, C. L.; Engelhard, M. H.; Thevuthasan, S.; Peden, C. H. F. Redox Properties of Water on the Oxidized And Reduced Surfaces Of $CeO_2(111)$. *Surf. Sci.* **2003**, *526*, 1−18.
(61) Chen, B.; Ma, Y.; Ding, L.; Xu, L.; Wu, Z.; Yuan, Q.; Huang, W. Reactivity of Hydroxyls and Water on a $CeO_2(111)$ Thin Film Surface: The Role of Oxygen Vacancy. *J. Phys. Chem. C* **2013**, *117*, 5800−5810.
(62) Lykhach, Y.; Johánek, V.; Aleksandrov, H. A.; Kozlov, S. M.; Happel, M.; Skála, T.; Petkov, P. S.; Tsud, N.; Vayssilov, G. N.; Prince, K. C.; et al. Water Chemistry on Model Ceria and Pt/Ceria Catalysts. *J. Phys. Chem. C* **2012**, *116*, 12103−12113.
(63) Herman, G. S.; Kim, Y. J.; Chambers, S. A.; Peden, C. H. F. Interaction of D_2O with $CeO_2(001)$ Investigated by Temperature-Programmed Desorption and X-ray Photoelectron Spectroscopy. *Langmuir* **1999**, *15*, 3993−3997.
(64) Senanayake, S. D.; Stacchiola, D.; Evans, J.; Estrella, M.; Barrio, L.; Pérez, M.; Hrbek, J.; Rodriguez, J. A. Probing The Reaction Intermediates For The Water−Gas Shift Over Inverse CeOx/Au(111) Catalysts. *J. Catal.* **2010**, *271*, 392−400.
(65) Henderson, M. A. The Interaction of Water with Solid Surfaces: Fundamental Aspects Revisited. *Surf. Sci. Rep.* **2002**, *46*, 1−308.
(66) Oliver, P. M.; Parker, S. C.; Mackrodt, W. C. Computer Simulation of the Crystal Morphology Of NiO. *Modell. Simul. Mater. Sci. Eng.* **1993**, *1*, 755.
(67) Davies, M. J.; Kenway, P. R.; Lawrence, P. J.; Parker, S. C.; Mackrodt, W. C.; Tasker, P. W. Impurity Segregation to the Surfaces of Corundum-Structured Oxides. *J. Chem. Soc., Faraday Trans. 2* **1989**, *85*, 555−563.
(68) Titiloye, J. O.; Parker, S. C.; Osguthorpe, D. J.; Mann, S. Predicting the Influence Of Growth Additives On The Morphology Of Ionic Crystals. *J. Chem. Soc., Chem. Commun.* **1991**, 1494−1496.
(69) Bhatta, U. M.; Reid, D.; Sakthivel, T.; Sayle, T. X. T.; Sayle, D.; Molinari, M.; Parker, S. C.; Ross, I. M.; Seal, S.; Möbus, G. Morphology and Surface Analysis of Pure and Doped Cuboidal Ceria Nanoparticles. *J. Phys. Chem. C* **2013**, *117*, 24561−24569.
(70) Wang, X.; Jiang, Z.; Zheng, B.; Xie, Z.; Zheng, L. Synthesis and Shape-Dependent Catalytic Properties of CeO_2 Nanocubes and Truncated Octahedra. *CrystEngComm* **2012**, *14*, 7579−7582.
(71) Liu, S. P.; Zhao, M.; Sun, G. E.; Gao, W.; Jiang, Q. Different Effects of Water Molecules on CO Oxidation With Different Reaction Mechanisms. *Phys. Chem. Chem. Phys.* **2018**, *20*, 8341−8348.
(72) Mai, H.-X.; Sun, L.-D.; Zhang, Y.-W.; Si, R.; Feng, W.; Zhang, H.-P.; Liu, H.-C.; Yan, C.-H. Shape-Selective Synthesis and Oxygen Storage Behavior of Ceria Nanopolyhedra, Nanorods, And Nanocubes. *J. Phys. Chem. B* **2005**, *109*, 24380−24385.
(73) Smith, L. R.; Sainna, M. A.; Douthwaite, M.; Davies, T. E.; Dummer, N. F.; Willock, D. J.; Knight, D. W.; Catlow, C. R. A.; Taylor, S. H.; Hutchings, G. J. Gas Phase Glycerol Valorization over Ceria Nanostructures with Well-Defined Morphologies. *ACS Catal.* **2021**, *11*, 4893−4907.
(74) Zabilskiy, M.; Djinović, P.; Tchernychova, E.; Tkachenko, O. P.; Kustov, L. M.; Pintar, A. Nanoshaped CuO/CeO_2 Materials: Effect of the Exposed Ceria Surfaces on Catalytic Activity in N_2O Decomposition Reaction. *ACS Catal.* **2015**, *5*, 5357−5365.
(75) Fu, Y.; Neal, C. J.; Kolanthai, E.; Munir, S.; Ta, K. M.; Molinari, M.; Seal, S. Effect of Acetate Ions and pH on the Morphology of Cerium Oxide Nanoparticles. *Colloids Surf. Physicochem. Eng. Aspects* **2023**, *679*, No. 132616.
(76) Florea, I.; Feral-Martin, C.; Majimel, J.; Ihiawakrim, D.; Hirlimann, C.; Ersen, O. Three-Dimensional Tomographic Analyses of CeO_2 Nanoparticles. *Cryst. Growth Des.* **2013**, *13*, 1110−1121.
(77) Wen, C.; Lu, M.; Zhao, M.; Zhu, J.; Li, M.; Shang, J.; Shan, Y.; Song, C. Co-Based Catalysts Supported on Ceria with Different Shape Structures for Hydrodeoxygenation of Guaiacol. *Energy Fuels* **2022**, *36*, 14986−14993.
(78) Eaimsumang, S.; Wongkasemjit, S.; Pongstabodee, S.; Smith, S. M.; Ratanawilai, S.; Chollacoop, N.; Luengnaruemitchai, A. Effect Of Synthesis Time on Morphology of CeO_2 Nanoparticles And Au/CeO_2 and their Activity in Oxidative Steam Reforming of Methanol. *J. Rare Earths* **2019**, *37*, 819−828.
(79) Aneggi, E.; Wiater, D.; De Leitenburg, C.; Llorca, J.; Trovarelli, A. Shape-Dependent Activity of Ceria In Soot Combustion. *ACS Catal.* **2014**, *4*, 172−181.
(80) Agrawal, R.; Peng, B.; Espinosa, H. D. Experimental-Computational Investigation of ZnO Nanowires Strength And Fracture. *Nano Lett.* **2009**, *9*, 4177−4183.
(81) Çakıroğlu, O.; Island, J. O.; Xie, Y.; Frisenda, R.; Castellanos-Gomez, A. An Automated System for Strain Engineering and Straintronics Of 2D Materials. *Adv.Mater. Technol.* **2023**, *8*, No. 2201091.
(82) Sayle, T. X. T.; Cantoni, M.; Bhatta, U. M.; Parker, S. C.; Hall, S. R.; Möbus, G.; Molinari, M.; Reid, D.; Seal, S.; Sayle, D. C. Strain and Architecture-Tuned Reactivity in Ceria Nanostructures; Enhanced Catalytic Oxidation of CO to CO_2. *Chem. Mater.* **2012**, *24*, 1811−1821.
(83) Brambila, C.; Nutter, J.; Molinari, M.; Sayle, D.; Sakthivel, T.; Seal, S.; Möbus, G. Void Space And Secondary Oriented Attachment Mechanisms In Cerium Oxide Nanorods. *J. Nanopart. Res.* **2022**, *24*, No. 227.
(84) Brambila, C.; Sayle, D. C.; Molinari, M.; Nutter, J.; Flitcroft, J. M.; Sayle, T. X. T.; Sakthivel, T.; Seal, S.; Möbus, G. Tomographic Study of Mesopore Formation in Ceria Nanorods. *J. Phys. Chem. C* **2021**, *125*, 10077−10089.
(85) Castanet, U.; Feral-Martin, C.; Demourgues, A.; Neale, R. L.; Sayle, D. C.; Caddeo, F.; Flitcroft, J. M.; Caygill, R.; Pointon, B. J.; Molinari, M.; Majimel, J. Controlling the {111}/{110} Surface Ratio of Cuboidal Ceria Nanoparticles. *ACS Appl. Mater. Interfaces* **2019**, *11*, 11384−11390.
(86) Sayle, T. X. T.; Molinari, M.; Das, S.; Bhatta, U. M.; Möbus, G.; Parker, S. C.; Seal, S.; Sayle, D. C. Environment-Mediated Structure, Surface Redox Activity And Reactivity Of Ceria Nanoparticles. *Nanoscale* **2013**, *5*, 6063−6073.

(87) Ijaz, S.; Ehsan, M. F.; Ashiq, M. N.; Karamat, N.; He, T. Preparation of CdS@CeO_2 Core/Shell Composite for Photocatalytic Reduction of CO_2 Under Visible-Light Irradiation. *Appl. Surf. Sci.* **2016**, *390*, 550−559.
(88) Han, C.; Yan, L.; Zhao, W.; Liu, Z. TiO_2/CeO_2 Core/Shell Heterojunction Nanoarrays for Highly Efficient Photoelectrochemical Water Splitting. *Int. J. Hydrogen Energy* **2017**, *42*, 12276−12283.
(89) Mitsudome, T.; Mikami, Y.; Matoba, M.; Mizugaki, T.; Jitsukawa, K.; Kaneda, K. Design of a Silver-Cerium Dioxide Core-Shell Nanocomposite Catalyst for Chemoselective Reduction Reactions. *Angew. Chem., Int. Ed.* **2012**, *51*, 136−139.

https://doi.org/10.1021/acs.jpcc.4c04172
J. Phys. Chem. C 2024, 128, 18451−18464